Journal of Biomedical Optics

SPIEDigitalLibrary.org/jbo

Femtosecond laser ablation of bovine cortical bone

Liliana T. Cangueiro
Rui Vilar
Ana M. Botelho do Rego
Vania S. F. Muralha

SPIE

Femtosecond laser ablation of bovine cortical bone

Liliana T. Cangueiro,[a] Rui Vilar,[a] Ana M. Botelho do Rego,[b] and Vania S. F. Muralha[c]
[a]Technical University of Lisbon, Instituto de Ciência e Engenharia de Materiais e Superfícies, IST, Avenida Rovisco Pais, 1049-001 Lisbon, Portugal
[b]Technical University of Lisbon, Centro de Química-Física Molecular and Institute of Nanoscience and Nanotechnology, IST, Avenida Rovisco Pais, 1049-001 Lisbon, Portugal
[c]Universidade Nova de Lisboa, VICARTE: Vidro e Cerâmica para as Artes, Faculdade de Ciências e Tecnologia, 2829-516 Monte de Caparica, Portugal

Abstract. We study the surface topographical, structural, and compositional modifications induced in bovine cortical bone by femtosecond laser ablation. The tests are performed in air, with a Yb:KYW chirped-pulse-regenerative amplification laser system (500 fs, 1030 nm) at fluences ranging from 0.55 to 2.24 J/cm^2. The ablation process is monitored by acoustic emission measurements. The topography of the laser-treated surfaces is studied by scanning electron microscopy, and their constitution is characterized by glancing incidence x-ray diffraction, x-ray photoelectron spectroscopy, Fourier transform infrared spectroscopy, and micro-Raman spectroscopy. The results show that femtosecond laser ablation allows removing bone without melting, carbonization, or cracking. The structure and composition of the remaining tissue are essentially preserved, the only constitutional changes observed being a reduction of the organic material content and a partial recrystallization of hydroxyapatite in the most superficial region of samples. The results suggest that, within this fluence range, ablation occurs by a combination of thermal and electrostatic mechanisms, with the first type of mechanism predominating at lower fluences. The associated thermal effects explain the constitutional changes observed. We show that femtosecond lasers are a promising tool for delicate orthopaedic surgeries, where small amounts of bone must be cut with negligible damage, thus minimizing surgical trauma. [DOI: 10.1117/1.JBO.17.12.125005]

Keywords: femtosecond laser; bone; surface modification; ablation.

Paper 12391 received Jun. 22, 2012; revised manuscript received Oct. 30, 2012; accepted for publication Oct. 30, 2012; published online Dec. 4, 2012.

1 Introduction

Minimally invasive surgery aims at minimizing the surgical trauma and reducing the patient's recovery time.[1] Lasers play an increasingly important role in this new approach to medical care, because they allow the noncontact cutting and removal of a wide variety of living tissues with extreme accuracy and reduced mechanical and thermal impacts, and they decrease the risk of collateral damage to peripheral structures such as nerves and blood vessels. Moreover, laser beams can be transported at distance by optical fiber and are essentially inertialess, facilitating remote operation by manipulators and robots. Lasers are also fully compatible with existing laparoscopic techniques and robotic surgery.[2] As a result, they are being actively investigated as a viable alternative to mechanical tools for delicate surgical applications at complicated anatomical locations, in particular for orthopaedic and cranio-maxillo-facial surgery.[3]

Bone is the main tissue in the skeletal system. It contains about 70% hydroxyapatite and 30% proteins (mainly collagen) and water. Its constitution is similar to that of dentin, but the two tissues present large differences in structure and functionality. Teeth consist mainly of intertubular dentin formed by a network of collagen fibers reinforced by hydroxyapatite nanocrystals, traversed by hollow cylindrical formations consisting of crystalline hydroxyapatite (peritubular dentin). Cells and blood vessels concentrate in the tooth central region, designated by pulp. Bone presents a much more complex structure; each bone includes a compact outer layer of cortical bone with porosity in the range of 5% to 30%, where hydroxyapatite nanocrystals surround the blood vessels, and an inner core of extremely porous cancellous bone (porosity 30% to 90%), consisting of a complex network of hydroxyapatite-rich plates and beams that limit cavities. These cavities are occupied by blood vessels and living cells.[4] In general, bone presents a larger content of living cells than dentin, enabling the tissue to regenerate itself continuously.

Lasers have been investigated for hard-tissue cutting and removal since 1964. Ruby,[5,6] CO_2,[7,8] Nd:YAG,[9] Ar^+,[10] Ho:YAG,[11] and alexandrite lasers[12] have all been tested for dentin removal without entirely fulfilling the existing expectations, in particular due to their low ablation rate and excessive heating of the tooth, potentially leading to carbonization, thermomechanical cracking, and, in extreme situations, necrosis.[12] These drawbacks can be overcome by using lasers favoring athermal instead of thermal ablation. Studies performed by our team[13] showed that dentin processed with 30 ns pulse duration, 248 nm wavelength excimer laser radiation presents no chemical or structural degradation. With these lasers, ablation is predominantly photochemical and, globally, heating is negligible. The reason for this behavior is that the ablation of intertubular dentin, the main constituent of the tooth bulk, is controlled by the photochemical decomposition of collagen, thus minimizing the thermal impact of the laser treatment on the material.[14,15] Unfortunately, the ablation rates achieved with these lasers are too low for practical applications, and their intense UV beams are a potential health hazard.[16] Er:YAG and Er,Cr:YSGG lasers (wavelengths of 2.94 μm and 2.78 μm, respectively) allow achieving higher ablation rates for dentin and are now extensively used in dentistry.[17–19] The radiation wavelengths of these lasers are within strong

Address all correspondence to: Rui Vilar, Technical University of Lisbon, Instituto de Ciência e Engenharia de Materiais e Superfícies, IST, Avenida Rovisco Pais, 1049-001 Lisbon, Portugal. Tel: (+351) 21 841 81 21; Fax: (+351) 21 841 81 20; E-mail: rui.vilar@ist.utl.pt.

0091-3286/2012/$25.00 © 2012 SPIE

absorption bands of water. As a result, radiation is efficiently absorbed by the water present in dentin. The water is suddenly evaporated, leading to a pressure pulse that mechanically disrupts the tissue.[20] The resulting removal rates are high, and thermal damage is low, as compared to other pulsed infrared lasers, but there are indications that, for certain parameter ranges, the mechanical shock may lead to subsuperficial cracking of dentin.[20,21]

Laser ablation of bone was less studied than the ablation of dentin, but since the constitution of the two tissues is similar, identical ablation behavior can be expected. CO_2 lasers originated severe charring in bone cutting experiments.[22] On the contrary, Er:YAG and Er,Cr:YSGG lasers were successfully tested for orthopaedic, maxillofacial, and periodontal surgery,[17–19] but thermal necrosis of the tissue was observed in some conditions.[23] Arguably, these detrimental effects can be overcome by using lasers with subpicosecond pulse duration,[24] because, at the high radiation intensities achieved with these lasers (larger than 10^{11} W/cm^2), multiphoton ionization becomes probable. The resulting free electrons are accelerated by the incoming radiation and collide with other atoms, initiating an avalanche effect that leads to the formation of a plasma and, eventually, to ablation.[24] Plasma-induced ablation of dentin allows relatively high ablation rates without melting or cracking and with negligible modification of the underlying tissue constitution.[25] Wieger, Zoppel, and Wintner[26] compared the ablation of cortical and cancellous bovine bone by Yb picosecond pulse duration and Er nanosecond pulse duration lasers and found numerous advantages in the first type of laser, namely high removal rates and absence of collateral damage such as melting, carbonization, and cracking. On the other hand, Leucht et al. observed[27] that the regeneration of a corticotomy performed with a Ti:Sapphire laser with a 1 ps pulse duration is faster than when the procedure was carried out by conventional saw cutting. The authors explained this difference by the absence of denaturation of the collagen of bone, which reduces the probability of inflammatory reactions.

Ultrafast lasers are promising tools for orthopaedic surgery, but we are still far from understanding femtosecond laser bone ablation mechanisms, and no detailed studies of the chemical and structural modifications induced in bone by the laser treatment exist up to the moment. The aim of the present work was to study the topography, structure, and constitution of bovine femoral bone surfaces treated with femtosecond infrared laser radiation. Samples of cortical bone were harvested and submitted to treatment with 500 fs, 1030 nm wavelength laser pulses. The surface topography of the treated surfaces was studied by scanning electron microscopy (SEM), and their constitution was investigated by glancing incidence x-ray diffraction[28] (GI-XRD), x-ray photoelectron spectroscopy[29] (XPS), Fourier transform infrared spectroscopy (FTIR), and micro-Raman spectroscopy[30] techniques, which were selected because they provide complementary information on material surface composition and structure. Acoustic emission measurements[31] were performed to detect the onset of the ablation process.

2 Materials and Methods

2.1 *Samples Preparation*

Fresh bovine cadaver femur was obtained from a local abattoir. The attached soft tissue and the periosteum were removed with a scalpel, and samples about $10 \times 10 \times 2$ mm^3 were cut from the bone mid-diaphysis with a hacksaw. In order to ensure the homogeneity of optical properties and a reproducible behavior in the ablation experiments, the surfaces to be tested, corresponding to the external side of the bone, were polished with a series of SiC papers with decreasing particle sizes (80, 320, 800, and 2400 grit) under flowing water. The samples were eventually water-rinsed and stored in distilled water up to the laser experiments. After the laser treatment, the samples were fixed by immersion in a 70% ethanol solution for 24 h and dehydrated by consecutive immersion for 1 h in three grades of ethanol with decreasing water concentration (20%, 10%, and 0%).

The laser treatments were performed in air using a Yb:KYW chirped-pulse-regenerative amplification laser system (s-Pulse HP model, Amplitude Systèmes, Bordeaux, France). The pulse duration was 500 fs, and the radiation wavelength was 1030 nm. The average pulse energy was varied in the range from 93 to 716 μJ. It was calculated from the average laser beam power, measured at a pulse frequency of 1 kHz with a Ophir Photonics model 10ASHV1.1 RoHS power meter (Jerusalem, Israel). The laser ablation experiments were carried out by translating the sample in relation to the stationary laser beam using a computer-controlled XY stage (PI miCos, Eschbach, Germany). The laser beam was perpendicular to the sample surface and focused by a 100 mm focal length lens. The sample surface was located 5 mm below the focal plane.

The ablated volumes were determined by numerical integration of 3D reconstructions of the ablation craters created by AliconaMeX® software (Alicona Imaging, Graz, Austria) from stereoscopic pairs of SEM images of the craters, taken with angles of 0 deg and 10 deg between the normal to the sample surface and the electron beam. These measurements were carried out on craters produced at a pulse frequency of 10 Hz, with radiation fluences (pulse energy by unit area) of 0.55, 0.82, and 1.09 J/cm^2 and a number of pulses varying between 20 and 500. Five craters were measured for each set of experimental parameters, allowing the estimation of a standard deviation for the ablated volume measurements, which is typically 9.5%. The ablation threshold was calculated on the basis of measurements of the diameter of craters produced with 5, 10, 15, and 100 laser pulses at a repetition rate of 10 Hz and with fluences between 0.68 and 2.24 J/cm^2. The measurements were carried out on SEM images using ImageJ software (National Institutes of Health, Bethesda, Maryland). Taking into consideration the asymmetry of the craters, four diameters were measured in different directions for each crater, and an average was calculated. Five measurements were performed for each set of laser pulse number and fluence. The ablation threshold was calculated using the D^2-method[32] described by Mannion et al. The basis of the method is as follows. Assuming that the laser beam has a Gaussian energy distribution, the fluence in a plane perpendicular to the laser beam is given by

$$\phi(r) = \phi_0 e^{-2r^2/w_0^2}, \tag{1}$$

where r is the distance to the spot center, and w_0 is the laser beam radius at e^{-2} of the maximum intensity. The maximum fluence (ϕ_0) and the laser pulse energy (E_p) can be related by

$$\phi_0 = \frac{2E_p}{\pi w_0^2}. \tag{2}$$

The authors demonstrated that the diameter of an ablation crater (D) produced with a Gaussian beam with radius w_0 is related with the maximum fluence (ϕ_0) by

$$D^2 = 2w_0^2 \ln\left(\frac{\phi_0}{\phi_{th}}\right), \quad (3)$$

where ϕ_{th} is the ablation threshold fluence. Since ϕ_0 increases linearly with the pulse energy [Eq. (2)], the Gaussian beam radius w_0 can be calculated from a plot of the square of the average crater diameter versus the logarithm of the pulse energy. The average fluence can then be calculated from the pulse energy and the laser beam radius at e^{-2}. Knowing this value, the ablation threshold for a given number of laser pulses can be determined by extrapolating to zero the linear plot of the square of the crater diameter (D) as a function of the logarithm of the fluence. Since the calculated ablation threshold values decreased as the number of laser pulses increased, indicating an incubation effect, the ablation threshold for a single pulse and the incubation factor were calculated as proposed by Jee, Becker, and Walser.[33] These authors showed that the ablation threshold for N laser pulses [$\phi_{th}(N)$] is related to the ablation threshold for a single pulse [$\phi_{th}(1)$] by

$$\phi_{th}(N) = \phi_{th}(1) \cdot N^{S-1} \quad (4)$$

$$N \cdot \phi_{th}(N) = \phi_{th}(1) \cdot N^{S}. \quad (5)$$

The incubation coefficient and the single-pulse ablation threshold can be determined from a plot of the accumulated fluence [$N \cdot \phi_{th}(N)$] as a function of the number of laser pulses. The ablation process was monitored by recording the intensity of the airborne acoustic shock wave generated during the laser experiments using an acoustic emission sensor (Model AM41, Physical Acoustics Corporation, Princeton Junction, New Jersey) with an operating frequency range from 39 to 42 kHz and a peak sensitivity of 0 dB Ref V/μbar @40 kHz. The sensor was placed at a distance of 10 cm from the laser spot, at an angle of 45 deg to the surface normal. To avoid random surface effects, the acoustic signal resulting from the first nine laser pulses were neglected; only the wave corresponding to the 10th laser pulse was analyzed.

Surface characterization was performed on 10×10 mm^2 laser-treated areas. The laser treatment was performed at a frequency of 10 Hz by moving the sample with a constant velocity of 0.2 mm/s under the stationary laser beam. Initially, a 10 mm movement in the XX direction was carried out. The sample was returned to the track origin after completion of the first linear displacement and moved 30% of the track width in the YY direction, and a new 10 mm scan was performed in the XX direction. This procedure was repeated until complete area coverage was achieved. The laser treatments were carried out with average fluences of 0.55, 0.82, 1.09, and 2.18 J/cm^2.

2.2 *Characterization Methods*

The surface topography was investigated by SEM in the secondary electron imaging mode using a JEOL 7001 (JEOL, Tokyo, Japan) field-emission gun scanning electron microscope operated at an electron acceleration voltage of 15 kV. To avoid charging effects, the samples were coated with a gold-palladium film by direct current sputtering prior to observation.

The surface constitution was investigated by GI-XRD, XPS, FTIR, and micro-Raman spectroscopy. Tests were performed on the laser-treated samples and on samples in the pristine condition for comparative purposes. Ten tests were carried out for each set of treatment parameters; the results achieved were similar within the limits of experimental error. GI-XRD was performed with a Siemens D 5000 diffractometer (Karlsruhe, Germany) using Cu K$_\alpha$ radiation and an incidence angle of 1 deg. The scanning range was from 20 deg to 60 deg, with an increment of 0.04 deg and an integration time of 15 s. FTIR spectroscopy was performed in attenuated total reflectance (ATR) mode using a Nicolet 5700 FTIR spectrometer (Thermo Electron Corporation, Waltham, Massachusetts) with a solid-substrate™ beam splitter and a deuterated triglycine sulfate thermoelectrically cooled (DTGS-TEC) detector. Spectra were recorded in the range of 7400 to 350 cm^{-1}, with a 4 cm^{-1} resolution, by accumulating 512 wavelength scans. Micro-Raman spectroscopy was carried out using a Horiba Jobin-Yvon LabRam 300 spectrometer (Kyoto, Japan) equipped with a solid-state laser operating at 532 nm. The laser beam was focused with a 50× objective lens. The laser beam power at the surface of the samples was varied with the aid of a set of neutral density filters (optical densities 0.6, 1, and 2). The system was calibrated to better than 1 cm^{-1} before the measurements using a silicon sample. The spectra were obtained with a laser beam power of 5 mW and an acquisition time of 100 s and recorded as extended scans. The exact band wave numbers were determined by fitting the experimental data with Gaussian-Lorentzian curves using the instrument LabSpec software. The spectra were normalized to the most intense band, at *ca.* 960 cm^{-1}. x-ray photoelectron spectroscopy was performed with a XSAM800 (KRATOS Analytical, Manchester, United Kingdom) dual anode XPS spectrometer. The spectra were recorded with Al K_α radiation ($h\nu = 1486.6$ eV) and a power of 120 W, in ultra high vacuum ($\approx 10^{-7}$ Pa) at room temperature, with a take-off angle (TOA) of 90 deg, in fixed analyzer transmission (FAT) operation mode, with high magnification and a pass energy equal to 20 eV, using a step of 0.1 eV. The spectra were analyzed with Vision software (KRATOS). Source satellites and a Shirley background were subtracted to all spectra. The experimental curves were fit with Gaussian-Lorentzian products using XPSPEAK Version 4.1 freeware. No external charge compensation was used: The charge shift was corrected using as reference the binding energy of aliphatic carbon centered at 285.00 eV. The spectra were quantified using the most intense peaks for each element studied.[34] The sensitivity factors used in the quantification were 0.25 for C 1s, 0.66 for O 1s, 0.42 for N 1s, 1.19 for Ca 2p, 3.5 for Mg 1s, and 0.354 for P 2p.

3 Results

3.1 *Ablation Threshold*

The ablation threshold was calculated using the D^2-method[32] described in Sec. 2. The variation of the square diameter of the craters as a function of laser fluence for 5, 10, 15, and 100 laser pulses is represented in the semilogarithmic plots of Fig. 1, together with linear fittings to the experimental data. The corresponding ablation thresholds, determined by extrapolating D^2 to zero, are 0.59 ± 0.08, 0.48 ± 0.06, 0.48 ± 0.06, and 0.32 ± 0.04 J/cm^2, respectively (R^2: 0.95%, 0.99%, 0.98%, and 0.91%). The incubation coefficient and the ablation threshold for a single pulse were determined from the plot of the accumulated fluence [$N \cdot \phi_{th}(N)$] as a function of the number of pulses depicted in Fig. 2 ($R^2 = 0.9998$) and are 0.81 ± 0.01 and 0.79 ± 0.04 J/cm^2, respectively.

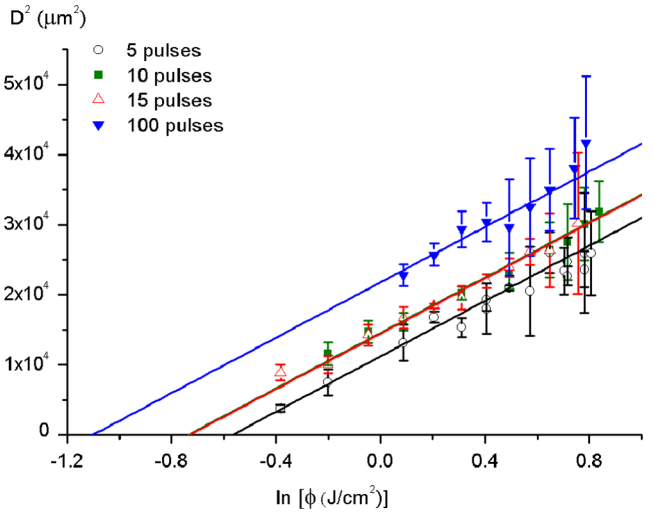

Fig. 1 Semilogarithmic plot of D^2 as a function of fluence. The lines are linear fitting of the experimental data.

A crater created by 30 laser pulses and 340 μJ pulse energy (average fluence 1.09 J/cm^2) and the corresponding depth profile are presented in Fig. 3. The ablated volume increases with the number of pulses up to a saturation value that increases with fluence (Fig. 4). The average saturation values, determined by averaging the ablation volume values for 200, 300, 400, and 500 laser pulses, are 1.8, 3.9, and 5.3×10^5 μm^3, respectively.

The variation of the maximum acoustic emission signal as a function of fluence is plotted in Fig. 5. Two variation regimes can be identified, both characterized by a logarithmic dependence of the acoustic signal on fluence. For fluences lower than 0.6 J/cm^2, the maximum acoustic emission intensity depends only weakly on fluence, the experimental data being adequately fitted by the equation $y = -473 + 258 \times \ln(x + 5.94)$ ($R^2 = 0.99$). For higher fluences, this dependence is more accentuated. The experimental data was fitted by the function $y = 47 + 78 \times \ln(x + 0.02)$ with $R^2 = 0.97$.

3.2 *Surface Morphology*

The topography of a cortical bone surface created by ablation with an average fluence of 1.09 J/cm^2 is depicted in the SEM micrograph of Fig. 6, which corresponds to a magnification of the crater in Fig. 3(a). The surface is flat, with an irregular and ragged appearance. The bone canaliculi are exposed, and the bone structure is preserved. No traces of resolidified material or cracks are observed. The surface is also free of major redeposited ablation debris or spallation ejecta created by mechanical disruption of the material by expanding gases due to water vaporization or tissue decomposition.

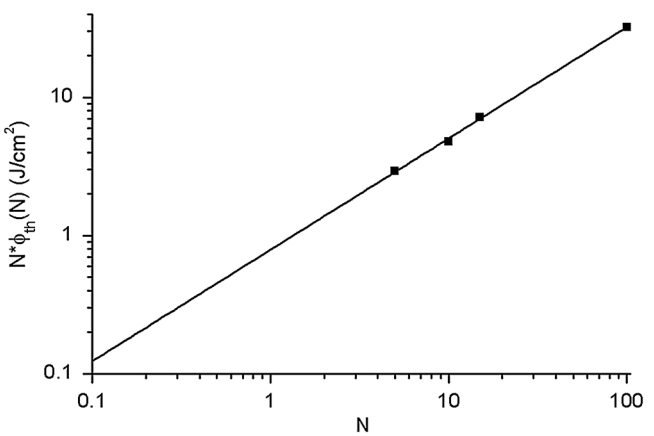

Fig. 2 Accumulated fluence as a function of the number of pulses. The solid line represents the fitting according to Eq. (5).

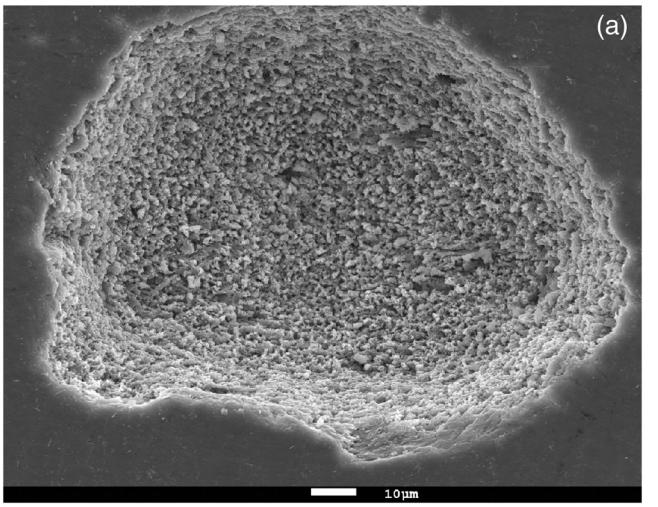

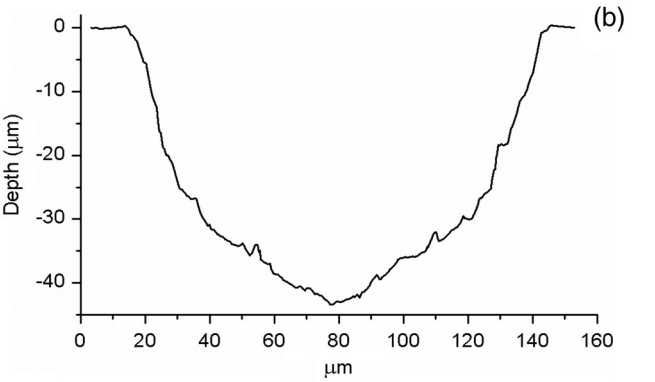

Fig. 3 Crater produced with a fluence of 1.09 J/cm^2 and 30 pulses at 10 Hz. (a) SEM image; (b) 2D profile.

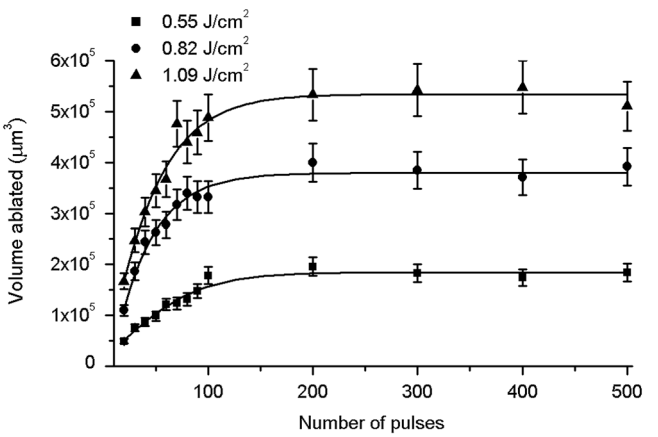

Fig. 4 Variation of the ablated volume as a function of the number of pulses (from 20 to 500). The curves result from a fitting to the experimental data and are a guide to the eye.

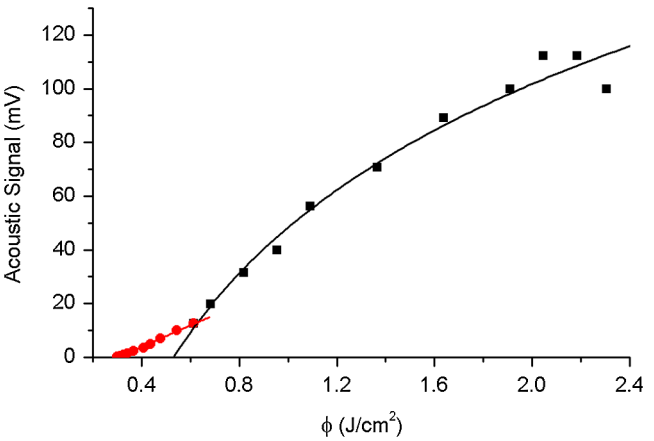

Fig. 5 Variation of the acoustic emission during the 10th laser pulse as a function of the radiation fluence.

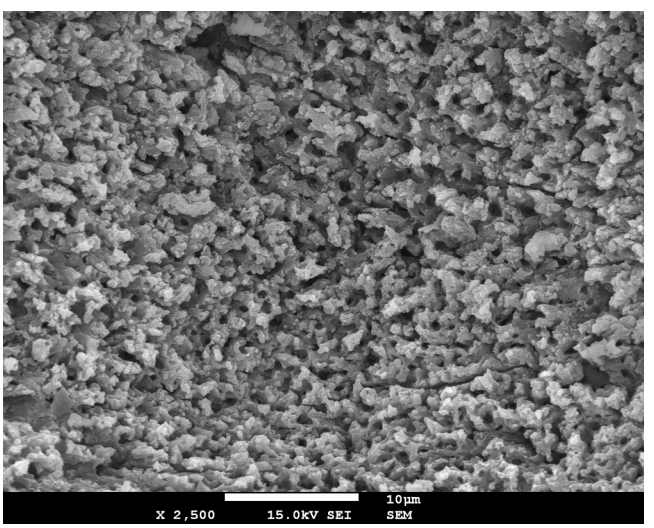

Fig. 6 Surface produced with a fluence of 1.09 J/cm^2 and 30 pulses at 10 Hz, corresponding to a magnification of the inside of the crater depicted in Fig. 3(a).

3.3 *Surface Composition*

3.3.1 *Fourier transform infrared spectroscopy*

The ATR-FTIR spectra of cortical bone in the untreated condition and after laser treatment with average fluences of 0.55, 0.82, and 2.18 J/cm^2 are represented in Fig. 7. The spectrum of the untreated sample has a higher signal-to-noise ratio than the laser-treated samples' spectra, because the sample was polished and presented higher reflectivity. The phosphate and carbonate absorption bands in these spectra are associated with the mineral phase of bone, a calcium-deficient hydroxyapatite. The most intense bands, associated with PO_4^{3-}, appear at 1010 and 956 cm^{-1} and correspond to the ν_3 antisymmetric PO stretching mode and the ν_1 symmetric stretching mode, respectively.[35] The absorption bands at 1415 and 1450 cm^{-1} can be attributed to the ν_3 mode of CO_3^{-2} substituted in B-type PO_4^{3-} and A-type OH^- anionic sites, respectively.[13,35] The band at 873 cm^{-1} is related to CO_3^{-2} ν_2 mode.[35] The organic constituents of the material are revealed by the bands of collagen, the main organic component of bone, between 1650 and 1200 cm^{-1}. The bands at 1680 to

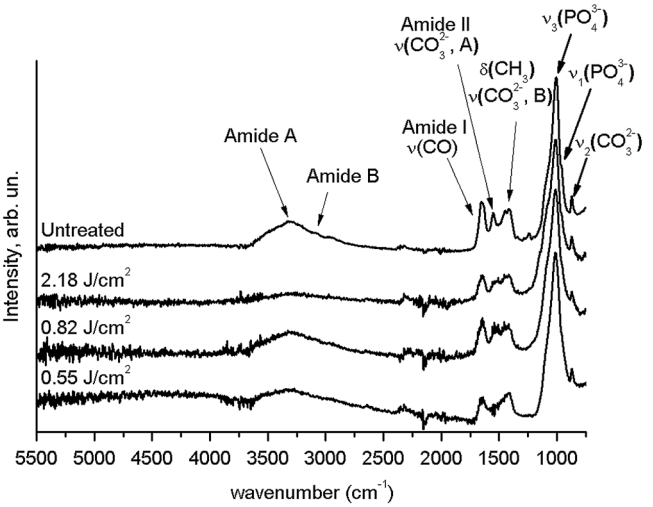

Fig. 7 FTIR spectra of treated and untreated samples.

1600 cm^{-1}, 1580 to 1510 cm^{-1}, and 1240 cm^{-1} are related to the amide I (C = O bond stretching), amide II (C-N bond stretching and N-H deformation modes), and amide III groups of the collagen molecule, respectively. The broad absorption band centered at 3320 cm^{-1} can be attributed to amide A group (N-H asymmetric stretching mode) of collagen, and the band at 3000 to 2900 cm^{-1} corresponds to the stretching of the CH_2 chain bonds.[36] Laser ablation leads to a decrease in the relative amplitude of the amide bands associated with collagen. The relative amplitude of the other IR absorption peaks, namely those associated with the mineral constituent of bone, is not significantly affected by the laser treatment.

3.3.2 *Micro-Raman spectroscopy*

The micro-Raman spectrum of a sample treated with 0.82 J/cm^2 is depicted in Fig. 8, together with the spectrum of an untreated sample. All the Raman bands observed in the laser-treated sample spectrum can be unequivocally assigned to bone's constituents, showing that no new phases formed due to the laser treatment. No peaks corresponding to amorphous carbon are observed (they should exist[37] at *ca.* 1580 and 1350 cm^{-1}), showing that no carbonization occurred. The spectra of Fig. 8(a) present the main phosphate ν_1 vibration band at *ca.* 960 cm^{-1} (the higher amplitude band) and the two main collagen bands, the amide I and III at *ca.* 1676 and 1247 cm^{-1}, the bending vibration band of the HPO_4^{2-} ion at *ca.* 1453 cm^{-1}, and the ν_1 vibration band of CO_3^{2-} at *ca.* 1070 cm^{-1} (Ref. 38). They are similar for both sample conditions. Figure 8(b) shows an expanded view of the overlapped CH vibration bands of the lipidic and proteic components of the tissue. The differences between the Raman spectra of untreated and treated samples are very small. The spectrum of the untreated sample presents a better signal-to-noise ratio in the collagen bands and a higher relative intensity of the ν_3 vibration band of the phosphate group at *ca.* 1004 cm^{-1} as compared to the laser-treated samples' spectrum, probably due to the different surface roughness of the samples. The most relevant difference between the spectra of the treated and untreated samples is the band at *ca.* 855 cm^{-1}, corresponding to the stretching mode of the aromatic C—C—H bonds,[38] which is present in the

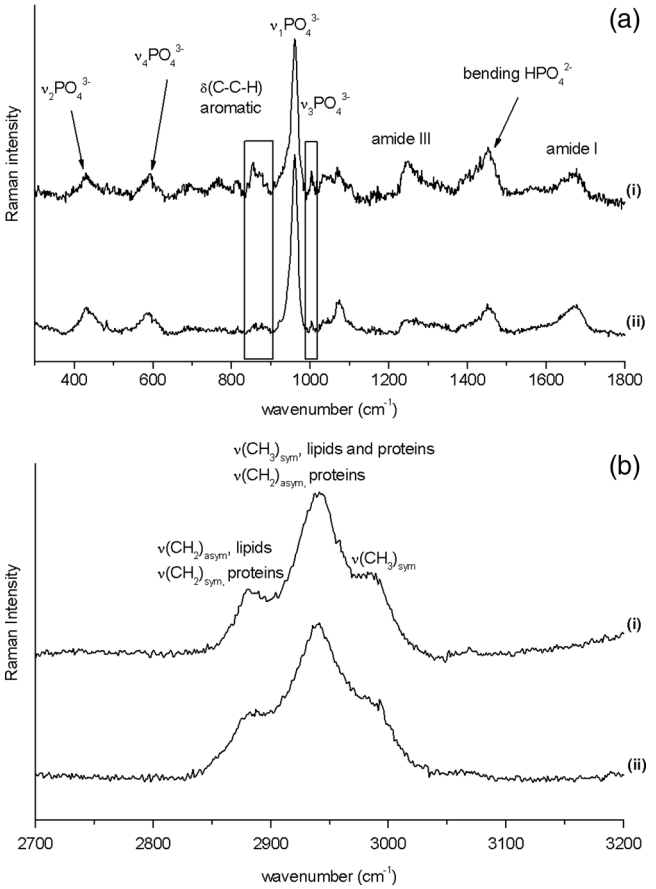

Fig. 8 Micro-Raman spectra of (a) the region between 400 and 1800 cm^{-1} from an untreated bone tissue sample (i) and treated bone tissue sample (ii); (b) the region between 2700 and 3200 cm^{-1} from an untreated bone tissue sample (i) and treated bone tissue sample (ii).

spectrum of the untreated sample and absent from the spectrum of the treated sample.

3.3.3 *X-ray diffraction*

The glancing-incidence x-ray diffractograms of cortical bone before and after laser treatment are shown in Fig. 9, together with a diffractogram of synthetic hydroxyapatite presented as a reference. All the diffraction peaks observed in bone diffractograms can be indexed as nonstoichiometric hydroxyapatite,[39] according to JCPDS card number 09-0432. The large width of the hydroxyapatite peaks in bone is consistent with the partially amorphous nature of the phase. The diffractograms of the samples treated with 0.82 and 1.09 J/cm^2 present a prominent narrow peak at 32.8 deg that can be indexed as the $(3\ \ 0\ \ 0)$ peak of hydroxyapatite and that is not observed in the diffractogram of the untreated sample.

3.3.4 *X-ray photoelectron spectroscopy*

The regions of the XPS spectra retained for analysis are those related to hydroxyapatite, i.e., the peaks associated to Ca 2p, O 1s, and P 2p (Fig. 10). The spectral regions corresponding to magnesium, an element that partially replaces calcium in the hydroxyapatite crystallographic structure of natural hard tissues,[40] are not described, because they did not provide relevant

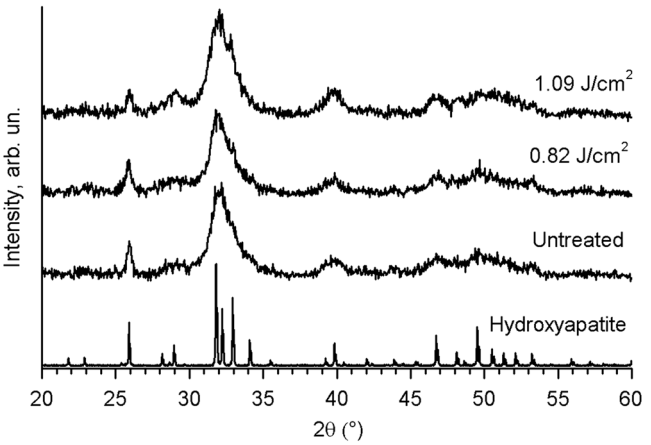

Fig. 9 X-ray diffractograms of treated and untreated bone samples and synthetic hydroxyapatite.

information, while the C 1s and nitrogen regions—originating from the collagen molecules—were considered only for energy calibration purposes, because carbon contamination precludes the quantification of these elements. The Ca 2p region of the spectra exhibits a single doublet both for the laser-treated and untreated samples. The main component of the doublet ($Ca\,2p_{3/2}$) is centered at a binding energy of 347.4 ± 0.1 eV, while its second component ($Ca\,2p_{1/2}$) has an orbit-spin shift of 3.6 ± 0.1 eV, as shown in Fig. 10(a). The P 2p peak consists of a single doublet, as well, with a separation of 0.9 ± 0.1 eV, the component $P\,2p_{3/2}$ being centered at 133.2 ± 0.1 eV, as shown in Fig. 10(b) and in agreement with the results of Sivakumar et al.[41] The O 1s region was fitted with a main component at 531.1 ± 0.1 eV, as shown in Fig. 10(c). This can be assigned to oxygen in the hydroxyapatite phosphate group and to oxygen from carbonyl groups. The second component is about 20% of the main one in the untreated region of the sample and decreases to less than 10% for the treated region. The main results of the quantitative analysis of the XPS spectra are presented in Table 1.

4 Discussion

The results described in Sec. 3 show that the threshold for the ablation of bovine cortical bone with 500 fs duration pulses of 1030 nm laser radiation decreases when the number of laser pulses increases (Table 2). This variation can be explained by the creation of defects at fluences lower than the single-pulse ablation threshold, which facilitates ablation by multiphoton excitation during subsequent laser pulses.[42] For infrared photons with energy lower than the energy gap of dielectrics, radiation absorption in perfect crystals can be achieved only by multiphoton absorption. However, it is often verified that laser irradiation at fluences lower than the ablation threshold, despite being insufficient to promote direct ablation during the first laser pulses, may act to create defects corresponding to energy levels within the gap that enhance radiation absorption by the material and facilitate ablation during subsequent laser pulses. Assuming that this mechanism was occurring, a value for the incubation coefficient of 0.81 ± 0.01 was calculated using the method proposed by Jee, Becker, and Walser.[33] This value is in good agreement with the one determined by Nicolodelli, Lizarelli, and Bagnato[43] for bovine femur bone treated with a Ti:Sapphire femtosecond with 70 fs pulse duration and 801 nm central emission wavelength ($S = 0.788 \pm 0.004$).

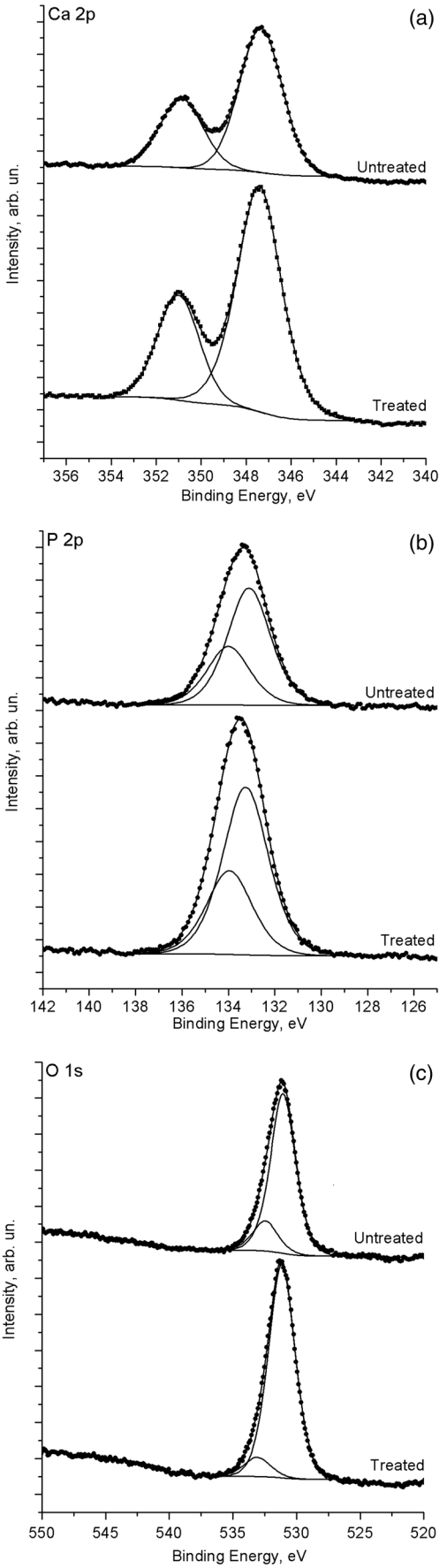

Fig. 10 Relevant regions of the XPS spectra of untreated and laser-treated cortical bone samples: (a) Ca 2p; (b) P 2p; (c) O 1.

Table 1 XPS atomic percentages and atomic ratios in the treated and untreated regions.

	Treated	Untreated
Ca	14.9	10.2
Mg	0.9	n.m.
P	9.7	7.0
$O_{531.1}$	42.3	33.1
$O_{532.7}$	3.8	6.3
N	5.0	7.7
C	23.4	35.6
Ca/P	1.54	1.46
$O_{531.1}$/P	4.4	4.7
(Ca + Mg)/P	1.64	

The single-pulse ablation threshold of cortical bone in the present experimental conditions is 0.79 ± 0.04 J/cm^2. This value is compared to those found in the literature in Table 3, which also includes the main processing parameters used by the different authors. The present value is in good agreement with the one determined by Wieger, Zoppel, and Wintner[26] for bovine cortical bone and by Girard et al.[44] for porcine cortical bone (0.69 ± 0.08 J/cm^2) and higher than the ablation threshold found by Poli[45] for rabbit cortical bone (0.54 J/cm^2). The ablation thresholds determined by Emigh et al.[46] for unpolished samples of porcine cortical bone and by Altman[47] for bovine femoral bone are much higher (3.29 and 2.6 J/cm^2, respectively). Taking into consideration that dentin has a constitution similar to that of bone, it is instructive to compare these values with those found for dental hard tissues, and the corresponding values were included in the table. Neev et al.[48] found 0.5 and 0.7 J/cm^2 for the ablation thresholds of dentin and enamel, respectively, using a laser with 350 fs pulse duration and 1050 nm wavelength, while Alves, Oliveira, and Vilar[25] found 0.6 ± 0.2 J/cm^2 for the ablation threshold of dentin in experimental conditions similar to those used in the present work. The lower ablation threshold value found by Poli[45] can probably be explained by the extremely low pulse duration of the laser used by this author (51 fs). The other values fall

Table 2 Ablation threshold for different numbers of laser pulses calculated using the D^2-method.

Number of pulses (N)	Calculated ablation threshold (J/cm^2)
1	0.79 ± 0.04
5	0.59 ± 0.08
10	0.48 ± 0.06
15	0.48 ± 0.06
100	0.32 ± 0.04

Table 3 Hard tissues' ablation threshold values obtained with ultrashort pulse duration lasers and their corresponding radiation wavelength.

Author	λ (nm)	Pulse duration (fs)	Ablation threshold (J/cm^2)	Hard tissue used
This work	1030	500	0.79 ± 0.04	Bovine cortical bone
Wieger et al. (see Ref. 26)	1040	330	0.78	Bovine cortical bone
Neev et al. (see Ref. 48)	1050	350	0.5	Human dentin
Alves et al. (see Ref. 25)	1030	500	0.6 ± 0.2	Human dentin
Poli (see Ref. 45)	800	51	0.54	Rabbit cortical bone
Girard et al. (see Ref. 44)	775	200	0.69 ± 0.08	Pig cortical bone
Altman (see Ref. 47)	800	150	2.6	Cortical bone
Emigh et al. (see Ref. 46)	800	170	3.29 ± 0.14	Pig cortical bone (unpolished)

into two classes, the first with values around 0.8 J/cm^2 and the second with values between 2.6 and 3.3 J/cm^2. Emigh et al.[46] explained the large ablation threshold found in their work by the fact that the samples used were not polished, so they presented lower reflectivity. However, this explanation does not apply to the results of Altman,[47] because this author used polished samples. A more plausible explanation results from the consideration of the spectral dependence of the optical properties of bone. The absorption coefficient of cortical bone for 800 and 1000 nm is 0.11 ± 0.02 and 0.22 ± 0.03 cm^{-1}, respectively.[49] As a result, the radiation absorption depth is smaller for 1000 nm than for 800 nm, leading to higher volumetric energy density. This difference is further enhanced when the radiation scattering is considered, as well.[24]

The ablated volume increases with number of pulses up to a saturation value (Fig. 4), and this saturation can be attributed to the progressive increase of the ablation crater depth and surface curvature with the increasing number of pulses, which leads to a continuous decrease of the fluence. The fact that no physicochemical or topographic alterations of the surface resulting from the laser treatment were observed can also explain this saturation effect.

The acoustic emission analysis revealed two regimes of variation of the maximum acoustic emission intensity with fluence. Both regimes are characterized by a logarithmic dependence of the acoustic signal on fluence, but for fluences lower than 0.6 J/cm^2, the maximum acoustic emission intensity shows a weak logarithmic dependence on fluence, while for higher fluences, this dependence is more accentuated. Nolte et al.[50] observed a similar behavior in the subpicosecond laser ablation of some metals and proposed a theoretical model explaining it. According to the authors, in the first regime, corresponding to the low-fluence range, ablation is controlled by the optical penetration depth of the material, while in the second one, ablation is determined by the effective heat penetration depth. However, in the present case, the low-fluence regime extends to fluences lower than the material ablation threshold for a similar number of pulses (0.48 ± 0.06 J/cm^2), so this regime cannot be associated with an ablative process. Instead, it may correspond to subablative thermal processes, such as the intense evaporation and desorption of volatile components, leading to the formation of a rapidly expanding gas plume[24,51] or to thermoelastic phenomena.[51,52] This interpretation is corroborated by the fact that the fluence found by extrapolating the curve fitted to the high-fluence regime data in Fig. 5 (0.53 J/cm^2) is similar to the 10 pulse ablation threshold calculated by the D^2-method (0.48 ± 0.06 J/cm^2, Table 2).

The ablation of cortical bone with femtosecond laser radiation leads to the formation of irregular and ragged surfaces, with no traces of melting or cracking. The diffraction peaks of hydroxyapatite in untreated cortical bone are much wider than those of synthetic crystallized hydroxyapatite, reflecting the partially amorphous nature of this mineral in bone and the extremely small size of the crystals (platelets with a diameter of 10 to 20 nm and less than 1 nm thick[53]). The width of most peaks remains unchanged by the laser treatment, but a prominent $(3\ \ 0\ \ 0)$ narrow peak appears at 32.8 deg, showing that the laser treatment led to the recrystallization of hydroxyapatite, forming larger crystals with the $(1\ \ 0\ \ 0)$ prismatic plane predominantly parallel to the sample surface. This alteration affects only a small volume of material, because no other changes are observed in the diffractograms. This is corroborated by the fact that the Ca/P ratio, determined by XPS analysis, is not affected by the laser treatment and remains similar to the theoretical value for stoichiometric hydroxyapatite. No significant changes were observed for the hydroxyapatite by FTIR and micro-Raman.

Analysis of the FTIR, micro-Raman, and XPS results shows that the laser treatment leads to a reduction of the proportion of organic compounds in the surface layer of the material. In the FTIR spectra, the relative amplitude of several bands is associated with collagen decreases, which also occurs in the aromatic C—H vibration bands in the Raman spectra. This may indicate that collagen is either partially denatured by the laser treatment (collagen can be denatured by exposition at temperatures as low as 40°C)[54,55] or partially eliminated from the surface due to the high temperatures attained during the ablative process. The decrease of the $O_{531.1}/P$ ratio observed by XPS analysis supports the latter hypothesis. The contribution of the carbonyl group oxygen to the $O_{531.1}$ peak decreases with the laser treatment, and the $O_{531.1}/P$ ratio tends to the stoichiometric ratio in the phosphate group ($O_{531.1}/P = 4$). Similarly, the amount of carbon decreases (Table 1), also corroborating this interpretation. The disappearance of organic compounds from the most superficial layer of material in the laser-treated samples should also be accentuated by the redeposition of ablation

debris, which must not contain carbon compounds, due to the high temperatures reached in the plume.

The XPS analysis shows that the Ca/P ratio at the sample surface is different from the stoichiometric value both in the untreated and treated samples, but the difference decreases with the laser treatment. This variation may be explained by the existence prior to the laser treatment of an organic overlayer at the sample surface, whose thickness is reduced by this treatment, as suggested by the carbon and nitrogen concentrations in Table 1. Since the kinetic energy of P 2p photoelectrons is higher than the kinetic energy of Ca 2p electrons, the Ca 2p photoelectrons are more attenuated than the P 2p ones by this organic overlayer. A reduction of its thickness due to the laser treatment would explain the observed variation. On the other hand, in natural hydroxyapatite, Ca can be replaced by Mg in some crystallographic positions.[56] If Mg is quantified, the ratio $(\mathrm{Mg}+\mathrm{Ca})/\mathrm{P}$ is similar to the stoichiometric one (1.6666) within the limits of the experimental error.

The present results can be compared with those achieved by precedent authors using micro- and nanosecond pulse duration lasers. Jovanovic et al.[57] observed surface carbonization and melting in bone samples ablated with a Ho:YAG laser ($\lambda = 2.1$ μm, pulse duration 500 μs) using fluences from 90 to 130 J/cm^2. This effect is less pronounced but still present when an Er:YSGG ($\lambda = 2.78$ μm, pulse duration 500 μs, fluence 55 J/cm^2) is used. This important thermal effect can be expected due to the large pulse duration and fluences used. Modern Er lasers do not present problems to the same extent.[19]

In a previous paper, the authors concluded that the ablation of dentin, using experimental conditions similar to the present ones, occurred by a combination of photothermal and electrostatic mechanisms.[25] The present results indicate that the same mechanism occurs for bone. According to Rode et al.,[58] subpicosecond laser ablation has the advantage that the heat conduction time and the electron-to-ion energy transfer time are longer than the pulse duration. If the pulse energy exceeds the energy required to ionize the target surface, electrons will be removed from the sample, leaving behind the cations and creating an electric field due to charge separation. When the energy of the escaping electrons is higher than the remaining material-binding energy, material will be athermally ablated by a mechanism that the authors designated by electrostatic ablation. Electrostatic ablation occurs for radiation intensities higher than the electrostatic ablation threshold (10^{13} to 10^{14} W/cm^2). If the absorbed power is lower than this threshold, the energy of the electrons is transferred to the lattice by electron-phonon interactions, and ablation occurs by a thermal mechanism, similar to the mechanism observed for nanosecond duration pulses and at a timescale that is orders of magnitude larger than the pulse duration. In actual practice, the spatial and temporal intensity distributions in the laser pulse result in a mixed interaction mode. In the present work, the intensities used were of the order of 10^{12} W/cm^2, so a partially thermal ablation mechanism is to be expected. This may explain the thermal effects observed. Despite this thermal contribution to ablation, deterioration of the bone structure and of the underlying material is negligible. Femtosecond laser ablation allows an accurate and clear removal of bone without any traces of surface melting, carbonization, and cracking, putting this type of laser in clear advantage as compared to Ho:YAG and Er lasers for clinical applications.

5 Conclusions

Laser ablation of cortical bone using an ultrafast laser with 500 fs pulse duration and 1030 nm wavelength and fluences higher than the ablation threshold allows controlled removal of bone with no evidence of melting, carbonization, or cracking. The ablated surfaces are flat, with an irregular and ragged appearance. The bone structure is preserved, and the surfaces are free of ablation debris. For the pulse fluences used (0.55 to 2.24 J/cm^2), ablation occurs by a combination of thermal and electrostatic mechanisms, the first mechanism predominating for lower fluences and the second one for higher fluences. This thermal mechanism leads to partial denaturation of collagen at the outermost layer of the remaining tissue. GI-XRD analysis suggests that some recrystallization of hydroxyapatite may also occur.

References

1. S. T. Canale, *Campbell's Operative Orthopaedics*, Mosby Elsevier, Philadelphia, Pennsylvania (2007).
2. J. Burgner, *Robot Assisted Laser Osteotomy*, KIT Scientific Publishing, Karlsruhe (2010).
3. S. Stubinger et al., "Er:YAG laser osteotomy: preliminary clinical and histological results of a new technique for contact-free bone surgery," *Eur. Surg. Res.* **42**(3), 150–156 (2009).
4. A. L. Boskey, "Mineralization of bones and teeth," *Elements* **3**(6), 387–393 (2007).
5. R. H. Stern and R. F. Sognnaes, "Laser beam effect on dental hard tissues," *J. Dent. Res.* **43**(5SP), 873–876 (1964).
6. L. Goldman et al., "Impact of laser on dental caries," *Nature* **203**(4943), 417 (1964).
7. O. R. Keller et al., "Laser-induced temperature changes in dentine," *J. Clin. Laser Med. Surg.* **21**(6), 375–381 (2003).
8. R. H. Stern, R. F. Sognnaes, and J. Vahl, "Lased enamel—ultrastructural observations of pulsed carbon-dioxide laser effects," *J. Dent. Res.* **51**(2), 455–460 (1972).
9. A. Aminzadeh, "FT-Raman spectroscopic studies of Nd/YAG laser—irradiated human dental enamel," *Iran J. Chem. Chem. Eng.-Int. Engl. Ed.* **21**(1), 44–46 (2002).
10. W. P. Kelsey, R. J. Blankenau, and G. L. Powell, "Application of the argon-laser to dentistry," *Lasers Surg. Med.* **11**(6), 495–498 (1991).
11. J. H. Kinney et al., "The threshold effects of Nd and Ho:YAG laser-induced surface modification on demineralization of dentin surfaces," *J. Dent. Res.* **75**(6), 1388–1395 (1996).
12. E. Steiger, N. Maurer, and G. Geisel, "Frequency-doubled alexandrite laser: an alternative dental device," *Proc. SPIE* **1880**, 149–155 (1993).
13. S. Eugenio et al., "Characterisation of dentin surfaces processed with KrF excimer laser radiation," *Biomaterials* **26**(33), 6780–6787 (2005).
14. M. Sivakumar et al., "Sealing of human dentinal tubules by KrF 248 nm laser radiation," *J. Laser Appl.* **18**(4), 330–333 (2006).
15. V. Oliveira, M. Sivakumar, and R. Vilar, "A mathematical description of surface texture development in laser-ablated dentin," *J. Appl. Phys.* **100**(10), 104701 (2006).
16. I. E. Kochevar, "Cyto-toxicity and mutagenicity of excimer laser-radiation," *Lasers Surg. Med.* **9**(5), 440–445 (1989).
17. K. U. Lewandrowski et al., "Use of the Er:YAG laser for improved plating in maxillofacial surgery: comparison of bone healing in laser and drill osteotomies," *Lasers Surg. Med.* **19**(1), 40–45 (1996).
18. S. R. Visuri, J. T. Walsh, and H. A. Wigdor, "Erbium laser ablation of dental hard tissue: effect of water cooling," *Lasers Surg. Med.* **18**(3), 294–300 (1996).
19. X. G. Wang, C. F. Zhang, and K. Matsumoto, "*In vivo* study of the healing processes that occur in the jaws of rabbits following perforation by an Er,Cr:YSGG laser," *Lasers Med. Sci.* **20**(1), 21–27 (2005).
20. D. C. Attrill et al., "Thermal effects of Er:YAG laser on a simulated dental pulp: a quantitative evaluation of the effects of a water spray," *J. Dent.* **32**(1), 35–40 (2004).

21. M. H. Niemz, *Laser-Tissue Interactions, Fundamentals and Applications*, Springer, Berlin, Heidelberg (2004).
22. M. Frentzen et al., "Osteotomy with 80-mu s CO2 laser pulses—histological results," *Lasers Med. Sci.* **18**(2), 119–124 (2003).
23. V. R. Geraldo-Martins et al., "Intrapulpal temperature during preparation with the Er:YAG laser: an *in vitro* study," *Photomed. Laser Surg.* **23**(2), 182–186 (2005).
24. A. Vogel and V. Venugopalan, "Mechanisms of pulsed laser ablation of biological tissues," *Chem. Rev.* **103**(5), 2079 (2003).
25. S. Alves, V. Oliveira, and R. Vilar, "Femtosecond laser ablation of dentin," *J. Phys. D: Appl. Phys.* **45**(24), 245401 (2012).
26. V. Wieger, S. Zoppel, and E. Wintner, "Ultrashort pulse laser osteotomy," *Laser Phys.* **17**(4), 438–442 (2007).
27. P. Leucht et al., "Accelerated bone repair after plasma laser corticotomies," *Ann. Surg.* **246**(1), 140–150 (2007).
28. P. Dutta, "Grazing incidence X-ray diffraction," *Curr. Sci.* **78**(12), 1478–1483 (2000).
29. C. D. Wagner et al., *Handbook of X-ray Photoelectron Spectroscopy*, Perkin Elmer Corp., Eden Prairie, MN (1978).
30. A. Carden and M. D. Morris, "Application of vibrational spectroscopy to the study of mineralized tissues (review)," *J. Biomed. Opt.* **5**(3), 259–268 (2000).
31. G. Chryssolouris, *Laser Machining: Theory and Practice*, Springer, New York (1991).
32. P. T. Mannion et al., "The effect of damage accumulation behaviour on ablation thresholds and damage morphology in ultrafast laser micromachining of common metals in air," *Appl. Surf. Sci.* **233**(1–4), 275–287 (2004).
33. Y. Jee, M. F. Becker, and R. M. Walser, "Laser-induced damage on single-crystal metal-surfaces," *J. Opt. Soc. Am. B* **5**(3), 648–659 (1988).
34. D. Briggs and J. T. Grant, *Surface Analysis by Auger and X-Ray Photoelectron Spectroscopy*, IM Publications, Chichester (2003).
35. I. Rehman and W. Bonfield, "Characterization of hydroxyapatite and carbonated apatite by photo acoustic FTIR spectroscopy," *J. Mater. Sci.-Mater. M.* **8**(1), 1–4 (1997).
36. M. C. Chang and J. Tanaka, "FT-IR study for hydroxyapatite/collagen nanocomposite cross-linked by glutaraldehyde," *Biomaterials* **23**(24), 4811–4818 (2002).
37. H. J. Scheibe, D. Drescher, and P. Alers, "Raman characterization of amorphous-carbon films," *Fresen. J. Anal. Chem.* **353**(5–8), 695–697 (1995).
38. G. Penel et al., "Composition of bone and apatitic biomaterials as revealed by intravital Raman microspectroscopy," *Bone* **36**(5), 893–901 (2005).
39. M. J. Glimcher, "Recent studies of the mineral phase in bone and its possible linkage to the organic matrix by protein-bound phosphate bonds," *Philos. Trans. R. Soc. London, Ser. B* **304**(1121), 479–508 (1984).
40. A. Bigi et al., "Chemical and structural characterization of the mineral phase from cortical and trabecular bone," *J. Inorg. Biochem.* **68**(1), 45–51 (1997).
41. M. Sivakumar et al., "KrF excimer laser processing of human enamel," *Mater. Sci. Forum*, **587–588**, 42–46 (2008).
42. D. Bäuerle, *Laser Processing and Chemistry*, 2nd ed., Springer, Berlin (1996).
43. G. Nicolodelli, R. D. Z. Lizarelli, and V. S. Bagnato, "Influence of effective number of pulses on the morphological structure of teeth and bovine femur after femtosecond laser ablation," *J. Biomed. Opt.* **17**(4), 048001 (2012).
44. B. Girard et al., "Effects of femtosecond laser irradiation on osseous tissues," *Lasers Surg. Med.* **39**(3), 273–285 (2007).
45. V. D. Poli, "Estudo da interação de pulsos de femtosegundos com tecido ósseo," Master Thesis, Fac. Odontologia USP (2006).
46. B. Emigh et al., "Porcine cortical bone ablation by ultrashort pulsed laser irradiation," *J. Biomed. Opt.* **17**(2), 8001 (2012).
47. K. J. Altman, "Microscale machining and mechanical characterization of bone tissue," Master Thesis, Ohio State University (2009).
48. J. Neev et al., "Ultrashort pulse lasers for hard tissue ablation," *IEEE J. Sel. Topics Quantum Electron.* **2**(4), 790–800 (1996).
49. A. N. Bashkatov et al., "Optical properties of human cranial bone in the spectral range from 800 to 2000 nm," *Proc. SPIE* **6163**, 616310 (2006).
50. S. Nolte et al., "Ablation of metals by ultrashort laser pulses," *J. Opt. Soc. Am. B* **14**(10), 2716–2722 (1997).
51. A. C. Tam, "Applications of photoacoustic sensing techniques," *Rev. Mod. Phys.* **58**(2), 381–431 (1986).
52. V. Venugopalan, N. S. Nishioka, and B. B. Mikic, "Thermodynamic response of soft biological tissues to pulsed infrared-laser irradiation," *Biophys. J.* **70**(6), 2981–2993 (1996).
53. S. J. Eppell et al., "Shape and size of isolated bone mineralites measured using atomic force microscopy," *J. Orthop. Res.* **19**(6), 1027–1034 (2001).
54. Z. K. Zhang, G. Y. Li, and B. Shi, "Physicochemical properties of collagen, gelatin and collagen hydrolysate derived from bovine limed split wastes," *J. Soc. Leath. Tech. Ch.* **90**(1), 23–28 (2006).
55. N. T. Wright and J. D. Humphrey, "Denaturation of collagen via heating: an irreversible rate process," *Annu. Rev. Biomed. Eng.* **4**, 109–128 (2002).
56. C. Y. C. Pak and E. C. Diller, "Ionic interaction with bone mineral. V. Effect of Mg2+, Citrate3-, F- and (SO4)2- on solubility, dissolution and growth of bone mineral," *Calcif. Tissue Res.* **4**(1), 69–77 (1969).
57. S. Jovanovic et al., "Effects of pulsed laser systems on stapes footplate," *Lasers Surg. Med.* **21**(4), 341–350 (1997).
58. A. V. Rode et al., "Subpicosecond laser ablation of dental enamel," *J. Appl. Phys.* **92**(4), 2153–2158 (2002).